Structure Design Enables Stable Anionic and Cationic Redox Chemistry in a T2-type Li-excess Layered Oxide Cathode

Xin Cao, *Haifeng Li*, *Yu Qiao*,* *Min Jia*, *Hirokazu Kitaura*, *Jianan Zhang, Ping He*, *Jordi Cabana and Haoshen Zhou**

X. Cao, Dr. Y. Qiao, Dr. M. Jia, Dr. H. Kitaura, Prof. H. Zhou
Energy Technology Research Institute, National Institute of Advanced Industrial Science and Technology (AIST), 1-1-1, Umezono, Tsukuba 305-8568, Japan.
E-mail: qiaoyu09206@163.com (Y. Q.); hs.zhou@aist.go.jp (H. Z.)

Dr. H. Li, Prof. J. Cabana
Department of Chemistry, University of Illinois at Chicago, Chicago, Illinois 60607, United States

Prof. P. He, Prof. H. Zhou
Center of Energy Storage Materials & Technology, College of Engineering and Applied Sciences, Jiangsu Key Laboratory of Artificial Functional Materials, National Laboratory of Solid State Microstructures, and Collaborative Innovation Center of Advanced Microstructures, Nanjing University, Nanjing 210093, P. R. China
E-mail: hszhou@nju.edu.cn (H. Z.)

X. Cao, Dr. M. Jia, Prof. H. Zhou
Graduate School of System and Information Engineering, University of Tsukuba, 1-1-1, Tennoudai, Tsukuba 305-8573, Japan

Prof. J. Zhang
College of Materials Science and Engineering, Zhengzhou University, Zhengzhou, 450001 P. R. China

Keywords: cathode materials, layered oxides, voltage decay, lattice oxygen release, structural stability

Coupled with anionic and cationic redox chemistry, Li-rich/excess cathode materials are prospective high-energy-density candidates for the next-generation Li-ion batteries. However, irreversible lattice oxygen loss would exacerbate irreversible transition metal migration, further resulting in a drastic voltage decay and capacity degeneration. Herein, a metastable layered Li-excess cathode material, T2-type $Li_{0.72}[Li_{0.12}Ni_{0.36}Mn_{0.52}]O_2$, was developed, in which the arrangement of oxygen stacking and alkali metal sites fundamentally differ from that in conventional O3-type layered structures. Benefiting from the stable structure evolution and Li migration processes, not only the voltage decay can be effectively restrained but also excellent capacity retention has been achieved during long term cycling. Moreover, irreversible/reversible anionic/cationic redox reactions have been systematically quantified via the combination of *in/ex-situ* spectroscopic techniques, further clarifying the charge compensation mechanism associated with (de)lithiation. These findings of the new T2 structure with the enhanced anionic redox stability will provide a new scope for the strategy of developing next-generation high-capacity Li-rich/excess oxides.

1. Introduction

Li-rich transition metal oxides with a general chemical formula of $xLi_2MnO_3 \cdot (1-x)LiTMO_2$ (TM = Mn, Ni, Co etc.) hold the greatest promise for the next-generation lithium-ion batteries due to their high energy density promoted by oxygen redox chemistry.[1] In typical layered Li-rich oxides (Li/TM >1 in formula), excess lithium ions substitute for sectional transition metals, forming Li_2MnO_3 domain with LiO_6 units in TM layer, which triggers remarkable oxygen-centered capacities in high-voltage regions.[2] However, these O3-type layered Li-rich cathodes suffer from rapid decay of both discharge capacity and operating voltage during cycling, which are ascribed to the irreversible lattice oxygen loss and derived structure distortion, further hindering the development of practical applications.[3] More specifically, gaseous oxygen release during charging process is extremely destructive against the reversibility of anionic/cationic redox reactions and structural stability.[4] Within most of layered Li-rich oxides such as O′3-type Li_2MnO_3 and O3-type $Li_{1.2}Ni_{0.2}Mn_{0.6}O_2$, the capacities triggered by initial oxygen activation (charging) cannot be effectively recovered during anionic reduction (discharging), generating severe decay of output capacity and over reduction of transition metals.[5] Moreover, lattice oxygen loss severely aggravates irreversible TM migration (from original TM layer to Li layer), resulting in a layered/spinel/disordered phase transition and consequent voltage decay during long-term cycling.[6]

To solve these intrinsic issues, numerous research works have been carried out via internal and external modification methods to improve the electrochemical/structural

stability of conventional O3-type layered Li-rich oxides.[1b, 7] For instance, the substitution or doping with metals forming highly covalent interactions can stabilize oxygen redox by strengthening the hybridization of O 2p orbitals with metal orbitals.[8] Moreover, surface coating has been demonstrated as an effective way to enhance the structural stability of electrode/electrolyte interfaces by constructing a protective layer, further suppressing gaseous oxygen release upon Li^+ deintercalation.[7c, 9] However, a less explored, yet potentially effective strategy would be to design alternative oxygen stacking arrangements and coordination environments that are less conducive to detrimental transitions; indeed, most of modifications to stabilize the anionic/cationic redox activities in Li-rich layered oxides are based on the O3-type structure.[10] Furthermore, the complex overlap voltage regions of anionic/cationic redox reactions shown in galvanostatic electrochemical curves further puzzle the clarification of the charge compensation mechanisms due to the lack of quantification analyses on irreversible/reversible oxygen/TM-centered redox reactions.[11]

In this study, we developed a metastable Li-excess orthorhombic T2-type $Li_{0.72}[Li_{0.12}Ni_{0.36}Mn_{0.52}]O_2$ cathode material by a facile ion-exchange method from a layered P2-type Na precursor. Unlike O3-type layered cathodes with ABCABC oxygen arrangement and octahedral site of alkali metal, the T2-type cathode displays ABB′A′ oxygen stacking sequence in a two-layer unit cell, in which Li ions occupy tetrahedral sites within the AM layer. Benefiting from a stable evolution of its phase transitions and reversible Li migration within this structure, limited voltage decay and excellent discharge capacity retention (capacity drop of 0.24% per cycle, 100 cycles at low

current density of 10 mA g^{-1}) was successfully achieved. Moreover, the capacity contributions of anionic/cationic redox reactions were quantified via the combination of hard X-ray absorption spectroscopy (XAS) and differential electrochemical mass spectroscopy (DEMS) as well as acid titrated gas chromatography mass spectrometry (AT-GCMS), demonstrating reversible anionic oxygen-centered and cationic TM-based redox reactions can be achieved during long-term cycling.

2. Results and Discussion

2.1 Synthesis, structural characterization and electrochemical performance

T2-type $Li_{0.72}[Li_{0.12}Ni_{0.36}Mn_{0.52}]O_2$ (labelled as LLNMO) was synthesized by chemical Li^+/Na^+ ion exchange from $Na_{0.72}[Li_{0.12}Ni_{0.36}Mn_{0.52}]O_2$ (Figure 1a). The Na-based precursor is verified as a prototypical P2-type oxide by General Structure Analysis System (GSAS) Rietveld refinement of its XRD pattern (Figure S1 and Table S1), in which the oxygen is stacked in an ABBA arrangement sequence and Na ions occupy prismatic sites within AM layer. The (1/3, 1/3, 0) superstructure peaks in 20-30° is absent, indicating the absence of ordering of Li/Mn(Ni) in the TMO_2 slabs.[12] In addition, the contents of cationic elements in synthesized $Na_{0.72}[Li_{0.12}Ni_{0.36}Mn_{0.52}]O_2$ were confirmed by inductively coupled plasma (ICP, Table S2). Moreover, the charge/discharge profiles of the Na precursor represent relatively reversible anionic/cationic redox behaviors during initial cycles, which is consistent with reported Li-excess Na-based compounds (Figure S2).[13] Here, the Li-excess state is represented

by the fact that Li ions are located within TM layer in both Li and Na layered compounds.

After the chemical Li^+/Na^+ ion exchange process, the Li-excess state and disordered Li/Ni/Mn arrangement in TM layer were well preserved.[14] Na^+ ions within the AM layers were substituted by Li^+ ions, resulting in a change in the coordination environment from the original prismatic site (P-site) to a unique tetrahedral site (T-site).[15] The (002) diffraction peak in XRD pattern of LLNMO was located at around 17.7° (Figure 1b), suggesting the P/T transition of coordination environment in LiO_2 slabs was complete because the characteristic peak of prismatic Na sites with shorter interlayer distance along c-axis direction could not be observed. Furthermore, the location of (002) peak is also lower than that of the layered characteristic (003) peak in conventional O3-type structures, indicating the coordination environment of Li sites is not octahedral.[16] According to Rietveld refinement results calculated by General Structure Analysis System (Figure 1b and Table S3), these experimental peaks can be well indexed with an orthorhombic T2-type arrangement with the space group *Cmca*, displaying both Li-excess state in TM layer and Li-deficient state within the AM layer. The difference between the experimental and standard reference (T2-type $Li_{2/3}Ni_{1/3}Mn_{2/3}O_2$ with the space group of *Cmca*) is the absence of superstructure peaks at 20-30°, verifying the disordered arrangement within the TM layer was also preserved in T2-type LLNMO. The T2-type structure has ABB′A′ oxygen stacking arrangement, which is an intermediate state during the phase transition from P2 to O2 phase with an oxygen stacking of ABCB. Both T2 and O2 structures in Li compounds can be achieved

from P2-type Na precursor with oxygen stacking of ABBA via ion exchange strategy. The O2 structure is achieved by gliding of the second layer from B to C, delivering the ABCB oxygen stacking and the octahedral sites for lithium ions. However, the T2 structure is achieved after gliding of the second layer by a smaller distance, half the small hexagonal lattice constant, resulting in lithium ions located in distorted tetrahedral sites. Therefore, the B′ represents the midpoint position between B and C site, and the A′ position is the midpoint between A and B sites, respectively. The calculated lattice parameters of LLNMO are a = 8.6033(5) Å, b = 4.9514(1) Å, c = 10.0530(8) Å, V = 428.249 $Å^3$ and $\alpha = \beta = \gamma = 90°$ with goodness-of-fitting parameters of χ^2 (1.76) and R_{wp} (5.412%). Lastly, the chemical formula of LLNMO was also confirmed by ICP (Table S4), demonstrating that the valence of Ni and Mn in the pristine state is +3 and +4, respectively.

The composition of LLNMO upon charge/discharge was tracked with galvanostatic cycling to evaluate the electrochemical reversibility during the first two Li^+ (de)intercalation processes (Figure 1c). Starting from oxidation, the electrochemical cell with LLNMO displayed two plateaus with an average voltage of 4.25 and 4.75 V, respectively, accumulating total capacities (138.5 mAh g^{-1}) equivalent to the removal of 0.45 mol of Li per mol of compound with a final composition of $Li_{0.387}Ni_{0.36}Mn_{0.52}O_2$. The corresponding charge capacity exceeded the theoretical capacity assuming only a contribution of the $Ni^{3+/4+}$ redox couple (110.2 $mAhg^{-1}$), indicating that oxygen-centered redox reactions were involved since Mn^{4+} cannot be further oxidized even at these high potentials in typical layered oxides. Upon reduction, the slope of the

potential-composition profile indicated additional Li ions inserted into the layered structure to reach a final composition of $Li_{0.989}Ni_{0.36}Mn_{0.52}O_2$, displaying a high output discharge capacity of ~184 mAh g^{-1}. This high capacity was largely maintained upon the second charge, with only a limited irreversible capacity (~7 $mAhg^{-1}$), implying high electrochemical reversibility within LLNMO after the first charge. Furthermore, high stability with limited voltage decay was also observed upon long-term cycling of LLNMO. At a low current density of 10 mA/g, a limited capacity decay of 0.24% per cycle with nearly 100% coulombic efficiency was obtained after 100 cycles at a wide potential window of 2.0-4.8 V (Figure 1d). Negligible voltage decay of 0.11 and 0.05 V was achieved in the two main electrochemical regions, around 3.55 and 2.75 V, respectively (Figure 1d. insert). These results indicate stable redox processes and excellent electrochemical reversibility can be realized within LLNMO during long-term cycling.

2.2 Reversible Structural Evolution

Operando XRD measurements were performed to evaluate the structural evolution of LLNMO upon the initial two delithiation/lithiation processes (Figure 2a and Figure S3). During the initial charging, the characteristic peaks of a phase with T2 stacking slightly shifted to lower angle and then rapidly disappeared, while a series of new well-resolved peaks arose at higher angle, corresponding to the transition of the oxide from T2 to O2 stacking and, thus, involving a change in Li coordination environment in the AM layer from tetrahedral to octahedral. The T2/O2 phase transition is commonly

observed in layered T2-type $LiTMO_2$ because the Li^+ removal leads to the gliding of the TMO_2 slabs during charging, so the oxygen stacking evolves from ABB′A′ (T2) to ABCB (O2).[16] The interlayer distance along c-axis direction is significantly decreased during the phase transition because the smaller octahedral LiO_6 unit occupies the AM layer. Upon further delithiation, the characteristic peaks of the O2 phase gradually shifted to higher angle owing to the shrinkage of the TM layer caused by oxidation of Ni^{3+} reaction, accompanied by further vacating of the AM sites with Li^+ deintercalation. Subsequently, the peak locations displayed asymmetric changes in low voltage region because of the combination of Mn^{4+} reduction reactions in later period of first discharge.

At the end of the first discharge, the O2 phase was preserved, with the peaks shifting back in a manner symmetric with charge, while the pristine T2 phase was not recovered. Two *ex-situ* XRD patterns corresponding LLNMO electrodes after the first charge and discharge displayed a hexagonal O2-type arrangement with the space group $P6_3mc$, which further demonstrates the irreversible phase transition from T2 to O2 phase during initial charging (Figure S4 and Table S5-S6). *Operando* XRD analysis conducted in the second cycle was also completely dominated by the evolution of the O2 phase of LLNMO electrode. Moreover, the structural evolution process during the second charge is the reverse of the first discharge and the second discharge process displays similar structural evolution relative to the initial discharge, indicating that the LLNMO electrode experiences a highly reversible phase transition process after the initial charge. The reversible structural evolution within LLNMO during subsequent

cycles provides a solid foundation for stable structural and electrochemical stability during long-term cycling.

To investigate the intrinsic reasons of structure evolution and the reversibility of oxygen redox reactions upon (de)lithiation processes, ^{7}Li solid state nuclear magnetic resonance (ssNMR) spectroscopy was performed during the initial two cycles (Figure 2b). It is an effective measurement to achieve explicit identification of Li^{+} local environment and reliable quantification at different lithium (de)intercalated states. Generally, the resonances at 1300∼1650 ppm can be assigned to hyperfine interactions of Li sites within the TM layers (Li^{TM}), whereas the resonance of Li ions in the AM layer (Li_{AM}) is located at the lower region of 500∼1000 ppm.[17] The sharp peaks located at around 0 ppm can be ascribed to diamagnetic impurity phases such as Li_2CO_3 and/or LiF , which stems from the formation of cathode-electrolyte interphase layers.[18] Moreover, the broad signals of main resonances and spinning sidebands were caused by the hyperfine interactions between unpaired electrons on TM metals and Li spins. For pristine T2 LLNMO, integration of the two broad resonances centered at 713 (shaded grey) and 1520 ppm (shaded blue) showed that 85.7 % Li are found in the AM layer and 14.3 % Li within the TM layer, respectively, which is consistent with our design formula of $Li_{0.72}[Li_{0.12}Ni_{0.36}Mn_{0.52}]O_2$. In detail, the three Li_{AM} peaks (Li_{Mn}, Li_{Ni} and Li_{Li}) originate from variations in the neighboring environments of Mn, Ni and Li, respectively. After charging, the intensity of the two broad Li resonances gradually decreased, which is consistent with the extraction of Li ions from the layered structure, leading to the gliding of the TMO_2 slabs and phase transition from T2 to O2 structure.

As a result, 0.387 mol Li still resides in AM layer, whereas all Li ions within TM layer disappear, resulting in 0.12 mol vacancy of Li in TM layer and formation of O2-type $Li_{0.387}[Vac_{0.12}Ni_{0.36}Mn_{0.52}]O_2$. After discharge to 2 V, 0.925 mol Li_{AM} (93.5 %) and 0.064 mol Li^{TM} (6.5 %) were recovered, indicating that Li (de)intercalation is a relatively reversible process both in AM and TM layers, delivering the formula of $Li_{0.925}[Li_{0.064}Vac_{0.056}Ni_{0.36}Mn_{0.52}]O_2$ despite limited vacancies within TM layer cannot be fully filled. On the contrary, O3-type Li-rich layered oxides suffer from irreversible Li (de)intercalation processes. In particularly, Li_2MnO_3 cathode shows significant lithium removal (up to 85%) from the lattice on the first-cycle charge, whereas up to 30% of the Li can be reinserted in the host lattice upon initial discharge, resulting in a large number of vacancies both in AM and TM layers.[19] As a result, the Li–O–Li configurations are seriously destroyed due to the majority of Li ions cannot be reinserted within TM layers, which severely limits the application of capacity triggered by oxygen redox reactions. Furthermore, these defects severely exacerbate irreversible TM migration from TM layer to AM layer, giving rise to destructive phase transition of layered to spinel even to disordered structures, which is directly related to structural and electrochemical fade mechanisms. Notably, for LLNMO, Li in TM layer disappeared again and the content of Li within AM layer increased to 0.395 mol after the second charge, delivering the similar chemical formula of $Li_{0.395}[Vac_{0.12}Ni_{0.36}Mn_{0.52}]O_2$ compared with the first charged state. It indicates more reversible Li migration evolutions both in TM and AM layers after the initial charge,

which provides solid foundation of stable oxygen redox reactions and structural stability within LLNMO during long-term cycling.

2.3 Valence State Analysis of Mn and Ni

To further quantify the redox changes at cationic centers and clarify the charge compensation mechanism in Li-excess LLNMO electrode during Li^+ (de)intercalation processes, Mn and Ni K-edge hard X-ray absorption spectroscopy (XAS) were employed (Figures 3a and 3b). The evolutions of the Mn and Ni oxidation states can be deduced from the variation in the threshold of the absorption edge at different charged states.[20] By comparison with the position of first inflection point above 6540 eV, the first derivative of these spectra can be used to clearly derive the trends in rising edge (Figures 3c and 3d), which arises from the electric dipole-allowed transition from 1s to 3p orbital. Upon oxidation of LLNMO to 4.8 V, compared with pristine state, the absorption edge of Ni K-edge shifted toward higher photon energy while there was almost no energy shift of the Mn rising edge, indicating an obvious increase in Ni oxidation state and, at most, a slight change of Mn valence during the initial charge process. Furthermore, the spectrum of Ni K-edge shifted back to the original position after discharged to 3.0 V and then experienced no virtual change from 3.0 to 2.0 V, reflecting a highly reversible redox process of Ni occurring primarily at high potential, with the metal not significantly involved in the capacities generated at lower potential. In contrast, an obvious shift of the Mn K-edge to lower energy can only be observed after discharge to 2.0 V, suggesting Mn-based reduction reactions primarily occurred

at low potential during discharging. Moreover, upon subsequent recharge to 4.8V, the absorption edge of Mn and Ni both shifted to higher photon energy, reaching a position similar to that of the first charged state, indicating they were both redox active. Thus, it is rational to deduce that Mn and Ni redox within LLNMO undergo a relatively reversible process after the first Li^+ deintercalation.

To gain further insight into these cationic reactions upon cycling, the oxidation state was estimated by applying the integral method first proposed by Dau et al.[21] To subsequently assess the existence anionic redox reactions, we compared the values of capacity associated with these redox changes with the total charge/discharge capacity (from electrochemical results, Figure 1c). Using appropriate references for the Mn/Ni K-edge, the integral method gives a linear relationship between oxidation states (+2, +3 and +4) and corresponding edge positions regardless of the edge shape (Figure 3e and 3f). This curve was used as calibration to extract approximate average Mn/Ni oxidation states of LLNMO from measured edge positions using the same method. The detailed data processing of standard references of Ni/Mn XAS spectra by integral method is also shown in Figures S5 and S6. Herein, the valence of Mn and Ni in LLNMO is +3.94 and +3.03 in the pristine state, respectively, in good agreement with our design and ICP results. Upon initial charging, the average Ni oxidation state is considerably increased to +3.53, delivering ~55 mAh g^{-1}. In contrast to Ni, it is abnormal that the oxidation state of Mn has a slight decrease during charging, indicating superoxo species and/or O_2 release enlists a partial reduction of neighboring Mn^{4+} to Mn^{3+} based on the reductive coupling mechanism.[8b] Clearly, the capacity accumulated upon this first

charge was too high to be explained by redox changes at the Ni centers. Therefore, oxygen-centered oxidation reactions (O^{2-} to O^{n-}/O_2, n<2) are proposed to contribute up to ~95 $mAhg^{-1}$ during initial charging.

Upon initial discharging, the oxidation state of Mn and Ni decreased to +3.54 and +2.99, corresponding to 52.46 and 59.43 $mAhg^{-1}$, respectively. Again, these values add to less than the observed capacity, suggesting that part of the discharge capacity is contributed by oxygen-centered reduction. An estimation based on the total capacity indicates up to 72 $mAhg^{-1}$ from oxygen redox, suggesting an irreversible capacity of ~23 mAh g^{-1} with respect to the activity ascribed to oxygen in the first charge. This difference might originate from side reactions such as oxygen release and/or electrolyte decomposition.

After recharging to 4.8 V, Mn and Ni was oxidized to values similar to the first charged state, demonstrating that the Mn/Ni redox reactions are reversible after the initial Li^+ deintercalation process. Estimations of the oxygen-centered oxidation by comparing total capacity to the observed oxidation of Mn and Ni brought about a value of ~74 $mAhg^{-1}$, which is roughly equivalent to the initial discharge capacity, implying oxygen redox reactions are also relatively reversible after first charging. As a result, the estimated capacity distributions of Ni/Mn-based and oxygen-centered redox reactions during the initial two cycles can be extracted (Figure S7), which is significant to understand the charge compensation mechanism in Li-rich oxides and underlying relationship between anionic and cationic redox reactions.

2.4 Analysis of Oxygen Behavior

The reversible/irreversible oxygen-centered redox behaviors within LLNMO are further assigned and quantified by a combination of *ex-situ* X-ray photoelectron spectroscopy (XPS) and *operando* differential electrochemical mass spectrometry (DEMS) as well as acid titrations-gas chromatography mass spectrometry (AT-GCMS) (Figures 4a-4e). These techniques are generally recognized as effective methods to accurately monitor and quantify oxygen-related species (especially for oxidized species and O_2). For the pristine LLNMO, the signal with lower binding energy of lattice oxygen (O^{2-}) is located at 529.5 eV. Moreover, the higher binding energy peaks can be typically identified as carbonate species (531.6 eV) and oxygenated species (533.1 eV) on the surface, respectively (Figure 4a).[22] Upon charging to 4.8 V, an obvious shoulder appears at around 530.7 eV, which is commonly ascribed to the formation of oxidized lattice oxygen (O^{n-}), indicating anionic redox reactions are triggered upon initial charging. Furthermore, the O^{n-} signal disappears after discharge to 3.0 V and cannot be detected at the end of discharge process (2.0 V), indicating oxidized lattice oxygen has been reduced to lattice oxygen in high voltage region. Notably, the O^{n-} peak can be probed again when the sample is recharged to 4.8 V, indicating a relatively reversible oxygen redox reaction within the initial two Li^+ (de)intercalation processes. Furthermore, Ar^+ etching was employed to investigate the changes in these signatures at a probing depth from several nanometers to ~100 nm. With increased etching time, O^{n-} peak can be continuously observed in the charged state and can be reduced to lattice

oxygen during discharging (Figure 4b and 4c), demonstrating the oxygen redox reactions are reversible at both on surface and interior of the materials. Piper et al. pointed out that the specific XPS signal might conceivably be attributed to the combination of irreversible TM reduction (O-TM^{2+}) and electrolyte decomposition species in the near-surface region.[23] However, the obvious shoulder located at 530.8 eV disappeared upon discharging, which would be inconsistent with the existence of irreversible formation of O–TM^{2+} signal. Therefore, the peak can be tentatively identified as the signal of oxidized lattice oxygen to explain the charge compensation mechanism, consistent with the estimations from XAS.

In terms of irreversible oxygen behavior, based on DEMS, only 126 μmol/g O_2 could be detected at the end of the initial charge owning to the severe shrink of O–O distance, delivering 13.55 $mAhg^{-1}$ based on a $4e^-$ process from lattice oxide to O_2 (Figure 4d). However, it is worth mentioning that there is no increase of gaseous oxygen release during the subsequent constant current-constant voltage (CC-CV) process. Irreversible oxygen release cannot be observed by *operando* DEMS in subsequent processes, including the second CC-CV time, suggesting more moderate oxygen behaviors can be triggered after initial charging. Besides, a small amount of CO_2 is also detected in the first two charges, which could arise from electrolyte degradation at high voltages or/and reaction with generated electron-depleted oxo species. The exact origin cannot be accurately established based on the data available.

AT-GCMS offers a complementary quantitative measure to assess the contributions of oxygen redox reactions, as reported in a previous study of Li-rich

cathode materials showing oxygen redox.[24] By quantifying the amount of O_2 evolved from electrodes after acid titrations, the capacity of oxygen oxidation reactions can be calculated based on the oxygen evolution reaction between H^+/H_2O and oxidized lattice oxygen.[25] Here these titrations demonstrate contributions from oxygen redox during first and second charging (71.35 and 73.94 mAh g^{-1}) and the oxidized oxygen has been completely reduced during discharging, which is in agreement with the O-related capacity contributions quantified by XAS (Figure 4e).

Altogether, benefiting from the combination of XAS and *operando* DEMS as well as AT-GCMS, the charge compensation mechanism within LLNMO electrode has been clarified by estimating the oxidation states of Ni/Mn and the capacity contribution of oxygen redox during the initial two cycles (Figure 4f). After an initial structural rearrangement (T2/O2 phase transition) and slight lattice oxygen loss (1.1 %), LLNMO harvests relatively reversible electrochemical processes centered at the TMs and lattice oxygen during subsequent cycles. It also displayed distinct capacity distributions of anionic redox reactions (40 %, ~72 mAh g^{-1}), mainly in the high-voltage region, and cationic redox reactions (60 %, ~112 mAh g^{-1}), in the whole potential window, during initial discharge, which is beneficial for clarifying the underlying relationship between TM-based and oxygen-related redox reactions in Li-rich oxides.

3. Conclusion

In this work, we developed a Li-excess T2-type $Li_{0.72}[Li_{0.12}Ni_{0.36}Mn_{0.52}]O_2$ as cathode material with the ABB′A′ oxygen stacking arrangement and tetrahedral alkali

metal site, which fundamentally resolve the inherent issues of oxygen loss and structural distortion in conventional Li-rich oxides. Benefitting from rational structure design of oxygen stacking arrangement, a relatively reversible Li migration process can be harvested both in AM and TM layer, which is distinctly demonstrated through ssNMR measurement. Not only the durative output capacities triggered by anionic redox reactions can be achieved due to stable Li–O–Li (Vac.) configurations, but also the layered/spinel phase transition caused by irreversible TM migration can be effectively suppressed because of the modified oxygen stacking sequence, which provides a solid foundation of excellent capacity retention and limited voltage decay upon long term cycling. Moreover, combined with systematic *in/ex-situ* spectroscopic characterization system (DEMS, hard XAS and AT-GCMS etc.), the irreversible/reversible TMs/O-related redox reactions have been distinctly assigned, clarifying the charge compensation mechanism of anionic/cationic redox reactions. Altogether, these findings of the novel T2 structural framework and optimized oxygen redox chemistry will offer further unexplored opportunities in securing next-generation Li-rich cathodes with unique structures and high energy density.

Supporting Information

Supporting Information is available from the Wiley Online Library or from the author.

Acknowledgements

X. C. and H. L. contributed equally to this work. This research was partially supported by the National Key Research and Development Program of China (2016YFB0100203) and the National Natural Science Foundation of China (21633003, U1801251). H. L. and J. C. were supported by the National Science Foundation under Grant No. DMR-1809372. This research used resources of the Advanced Photon Source, a U.S. Department of Energy (DOE) Office of Science User Facility operated for the DOE Office of Science by Argonne National Laboratory under Contract No. DE-AC02-06CH11357. We thank Advanced Photon Source at Argonne National Laboratory. X. C. acknowledges the scholarship from the China Scholarship Council (CSC).

Received: ((will be filled in by the editorial staff))
Revised: ((will be filled in by the editorial staff))
Published online: ((will be filled in by the editorial staff))

References

[1] a) G. Assat, J.-M. Tarascon, *Nat. Energy* **2018**, *3*, 373–386; b) W. Lee, S. Muhammad, C. Sergey, H. Lee, J. Yoon, Y. M. Kang, W. S. Yoon, *Angew. Chem. Int. Ed.* **2020**, *59*, 2578-2605.

[2] a) K. A. Jarvis, Z. Deng, L. F. Allard, A. Manthiram, P. J. Ferreira, *Chem. Mater.* **2011**, *23*, 3614-3621; b) S. Zhao, K. Yan, J. Zhang, B. Sun, G. Wang, *Angew. Chem. Int. Ed.* **2020**, 202000262.

[3] a) L. Gu, D. Xiao, Y. S. Hu, H. Li, Y. Ikuhara, *Adv. Mater.* **2015**, *27*, 2134-2149; b) D. Mohanty, A. S. Sefat, J. Li, R. A. Meisner, A. J. Rondinone, E. A. Payzant, D. P. Abraham, D. L. Wood Iii, C. Daniel, *Phys. Chem. Chem. Phys.* **2013**, *15*, 19496-19509.

[4] a) R. A. House, G. J. Rees, M. A. Pérez-Osorio, J.-J. Marie, E. Boivin, A. W. Robertson, A. Nag, M. Garcia-Fernandez, K.-J. Zhou, P. G. Bruce, *Nat. Energy* **2020**; b) J. Lee, J. K. Papp, R. J. Clément, S. Sallis, D.-H. Kwon, T. Shi, W. Yang, B. D. McCloskey, G. Ceder, *Nat. Commun.* **2017**, *8*, 981; c) J. Hwang, S. Myeong, W. Jin, H. Jang, G. Nam, M. Yoon, S. H. Kim, S. H. Joo, S. K. Kwak, M. G. Kim, J. Cho, *Adv. Mater.* **2020**, 2001944; d) M. B. Yahia, J. Vergnet, M. Saubanère, M.-L. Doublet, *Nat. Mater.* **2019**, *18*, 496–502.

[5] a) K. Nakayama, R. Ishikawa, S. Kobayashi, N. Shibata, Y. Ikuhara, *Nat. Commun.* **2020**, *11*, 4452; b) J. Rana, M. Stan, R. Kloepsch, J. Li, G. Schumacher, E. Welter, I. Zizak, J. Banhart, M. Winter, *Adv. Energy Mater.* **2014**, *4*, 1300998; c) F. Wu, G.-T. Kim, T. Diemant, M. Kuenzel, A. R. Schür, X. Gao, B. Qin, D. Alwast, Z. Jusys, R. J. Behm, D. Geiger, U. Kaiser, S. Passerini, *Adv. Energy Mater.* **2020**, *10*, 2001830.

[6] a) A. Boulineau, L. Simonin, J. F. Colin, C. Bourbon, S. Patoux, *Nano Lett.* **2013**, *13*, 3857-3863; b) M. Gu, I. Belharouak, J. Zheng, H. Wu, J. Xiao, A. Genc, K. Amine, S. Thevuthasan, D. R. Baer, J.-G. Zhang, N. D. Browning, J. Liu, C. Wang, *ACS Nano* **2013**, *7*, 760–767.

[7] a) B. Xiao, H. Liu, N. Chen, M. N. Banis, H. Yu, J. Liang, Q. Sun, T. K. Sham, R. Li, M. Cai, G. Botton, X. Sun, *Angew. Chem. Int. Ed.* **2020**; b) F. Wu, G. T. Kim, T. Diemant, M. Kuenzel, A. R. Schür, X. Gao, B. Qin, D. Alwast, Z. Jusys, R. J. Behm, D. Geiger, U. Kaiser, S. Passerini, *Adv. Energy Mater.* **2020**, 2001830; c) Y. Lei, J. Ni, Z. Hu, Z. Wang, F. Gui, B. Li, P. Ming, C. Zhang, Y. Elias, D. Aurbach, Q. Xiao, *Adv. Energy Mater.* **2020**, 2002506; d) P. Liu, H. Zhang, W. He, T. Xiong, Y. Cheng, Q. Xie, Y. Ma, H. Zheng, L. Wang, Z. Z. Zhu, Y. Peng, L. Mai, D. L. Peng, *J. Am. Chem. Soc.* **2019**, *141*, 10876-10882.

[8] a) M. Saubanere, E. McCalla, J. M. Tarascon, M. L. Doublet, *Energy Environ. Sci.* **2016**, *9*, 984-991; b) M. Sathiya, G. Rousse, K. Ramesha, C. P. Laisa, H. Vezin, M. T. Sougrati, M. L. Doublet, D. Foix, D. Gonbeau, W. Walker, A. S. Prakash, M. Ben Hassine, L. Dupont, J. M. Tarascon, *Nat. Mater.* **2013**, *12*, 827-835; c) A. J. Perez, Q. Jacquet, D. Batuk, A. Iadecola, M. Saubanère, G. Rousse, D. Larcher, H. Vezin, M.-L. Doublet, J.-M. Tarascon, *Nat. Energy* **2017**, *2*, 954-962; d) H. Li, S. Ramakrishnan, J. W. Freeland, B. D. McCloskey, J. Cabana, *J. Am. Chem. Soc.* **2020**; e) X. Cao, H. Li, Y. Qiao, X. Li, M. Jia, J. Cabana, H.

Zhou, *Adv. Energy Mater.* **2020**, 1903785.

[9] a) G. Sun, F. D. Yu, C. Zhao, R. Yu, S. Farnum, G. Shao, X. Sun, Z. B. Wang, *Adv. Funct. Mater.* **2020**, 2002643; b) C. Cui, X. Fan, X. Zhou, J. Chen, Q. Wang, L. Ma, C. Yang, E. Hu, X. Q. Yang, C. Wang, *J. Am. Chem. Soc.* **2020**; c) Q. Chen, Y. Pei, H. Chen, Y. Song, L. Zhen, C. Y. Xu, P. Xiao, G. Henkelman, *Nat. Commun.* **2020**, *11*, 3411; d) X. D. Zhang, J. L. Shi, J. Y. Liang, Y. X. Yin, J. N. Zhang, X. Q. Yu, Y. G. Guo, *Adv. Mater.* **2018**, *30*, 1801751; e) J. Zheng, M. Gu, J. Xiao, B. J. Polzin, P. Yan, X. Chen, C. Wang, J.-G. Zhang, *Chem. Mater.* **2014**, *26*, 6320-6327; f) K. A. Kurilenko, O. A. Shlyakhtin, D. I. Petukhov, A. V. Garshev, *Solid State Ion.* **2018**, *324*, 59-64; g) R.-P. Qing, J.-L. Shi, D.-D. Xiao, X.-D. Zhang, Y.-X. Yin, Y.-B. Zhai, L. Gu, Y.-G. Guo, *Adv. Energy Mater.* **2016**, *6*, 1501914; h) S. Kim, W. Cho, X. Zhang, Y. Oshima, J. W. Choi, *Nat. Commun.* **2016**, *7*, 13598.

[10] D. Eum, B. Kim, S. J. Kim, H. Park, J. Wu, S. P. Cho, G. Yoon, M. H. Lee, S. K. Jung, W. Yang, W. M. Seong, K. Ku, O. Tamwattana, S. K. Park, I. Hwang, K. Kang, *Nat. Mater.* **2020**, *19*, 419–427.

[11] H. Chen, M. S. Islam, *Chem. Mater.* **2016**, *28*, 6656-6663.

[12] a) Y. Zou, B. Li, J. Ning, W. Chu, H. Zhang, R. Zou, D. Xia, *Adv. Mater.* **2018**, *30*, 1707255; b) F. Ning, B. Li, J. Song, Y. Zuo, H. Shang, Z. Zhao, Z. Yu, W. Chu, K. Zhang, G. Feng, X. Wang, D. Xia, *Nat. Commun.* **2020**, *11*, 4973.

[13] X. Cao, X. Li, Y. Qiao, M. Jia, F. Qiu, Y. He, P. He, H. Zhou, *ACS Energy Lett.* **2019**, *4*, 2409-2417.

[14] D. L. J. M. Paulsen, and J. R. Dahn, *J. Electrochem. Soc.* **2000**, *147*, 2862-2867.

[15] a) R. A. D. J. M. Paulsen, and J. R. Dahn, *Chem. Mater.* **2000**, *12*, 2257-2267; b) Z. Lu, J. R. Dahn, *Chem. Mater.* **2001**, *13*, 1252-1257.

[16] Y. Shao-Horn, F. Weill, L. Croguennec, D. Carlier, M. Ménétrier, C. Delmas, *Chem. Mater.* **2003**, *15*, 2977–2983.

[17] X. Li, M. Tang, X. Feng, I. Hung, A. Rose, P.-H. Chien, Z. Gan, Y.-Y. Hu, *Chem. Mater.* **2017**, *29*, 8282-8291.

[18] E. Salager, V. Sarou-Kanian, M. Sathiya, M. Tang, J.-B. Leriche, P. Melin, Z. Wang, H. Vezin, C. Bessada, M. Deschamps, J.-M. Tarascon, *Chem. Mater.* **2014**, *26*, 7009-7019.

[19] F. Dogan, J. R. Croy, M. Balasubramanian, M. D. Slater, H. Iddir, C. S. Johnson, J. T. Vaughey, B. Key, *J. Electrochem. Soc.* **2014**, *162*, A235-A243.

[20] M. Oishi, T. Fujimoto, Y. Takanashi, Y. Orikasa, A. Kawamura, T. Ina, H. Yamashige, D. Takamatsu, K. Sato, H. Murayama, H. Tanida, H. Arai, H. Ishii, C. Yogi, I. Watanabe, T. Ohta, A. Mineshige, Y. Uchimoto, Z. Ogumi, *J. Power Sources* **2013**, *222*, 45-51.

[21] H. Dau, P. Liebisch, M. Haumann, *Anal. Bioanal. Chem.* **2003**, *376*, 562-583.

[22] G. Assat, A. Iadecola, D. Foix, R. Dedryvère, J.-M. Tarascon, *ACS Energy Lett.* **2018**, *3*, 2721-2728.

[23] Z. W. Lebens-Higgins, H. Chung, M. J. Zuba, J. Rana, Y. Li, N. V. Faenza, N. Pereira, B. D McCloskey, F. Rodolakis, W. Yang, M. S. Whittingham, G. G. Amatucci, Y. S. Meng, T. L. Lee, L. F. J. Piper, *J. Phys. Chem. Lett.* **2020**, *11*,

2106−2112.
[24] S. E. Renfrew, B. D. McCloskey, *ACS Appl. Energy Mater.* **2019**, *2*, 3762-3772.
[25] J. Rana, J. K. Papp, Z. Lebens-Higgins, M. Zuba, L. A. Kaufman, A. Goel, R. Schmuch, M. Winter, M. S. Whittingham, W. Yang, B. D. McCloskey, L. F. J. Piper, *ACS Energy Lett.* **2020**, *5*, 634-641.

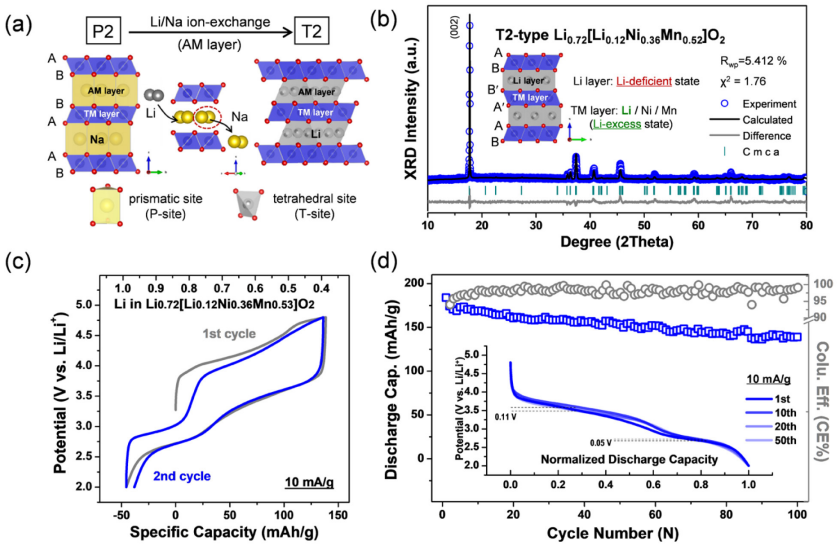

Figure 1. Synthesis, structural characterization and electrochemical performance of T2-type LLNMO. (a) Schematic illustration of Li/Na ion exchange reaction from P2-type Na-based precursor to T2-type Li-based LLNMO. (b) The XRD patterns of pristine T2-type LLNMO. The observed pattern, the calculated pattern, the difference between the two patterns and the corresponding Bragg positions are shown. The inset is a schematic illustration of the crystal structure of the LLNMO with ABB′A′ oxygen stacking along the [110] zone axis. (c) Typical charge–discharge profiles of LLNMO within the voltage window of 2.0 to 4.8 V at a current density of 10 mA g^{-1} in Li-half cells. The mole numbers of electron were converted to mole numbers of (de)intercalated Li^+ during the initial two cycles. (d) Cycling performance of LLNMO between 2 and 4.8 V at the current density of 10 mA g^{-1}. The inset displays the normalized discharge profiles of LLNMO in the 1st, 10th, 20th and 50th cycles.

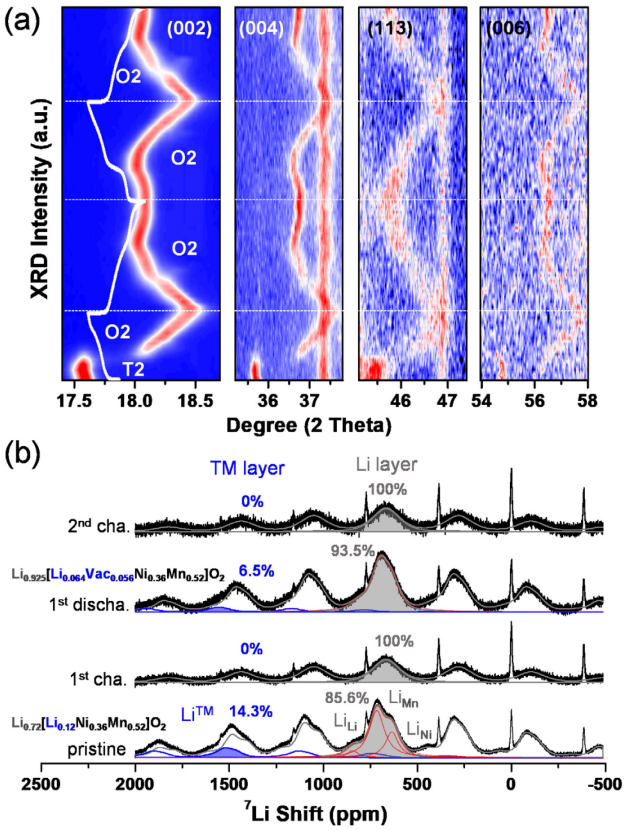

Figure 2. Phase evolution and Li migration processes of T2-type LLNMO during cycling. (a) In-situ XRD patterns of LLNMO electrode during the initial two cycles. ((b) ^{7}Li solid state NMR spectra of T2-type LLNMO electrode samples of pristine state, initial charge to 4.8 V and initial discharge to 2 V.

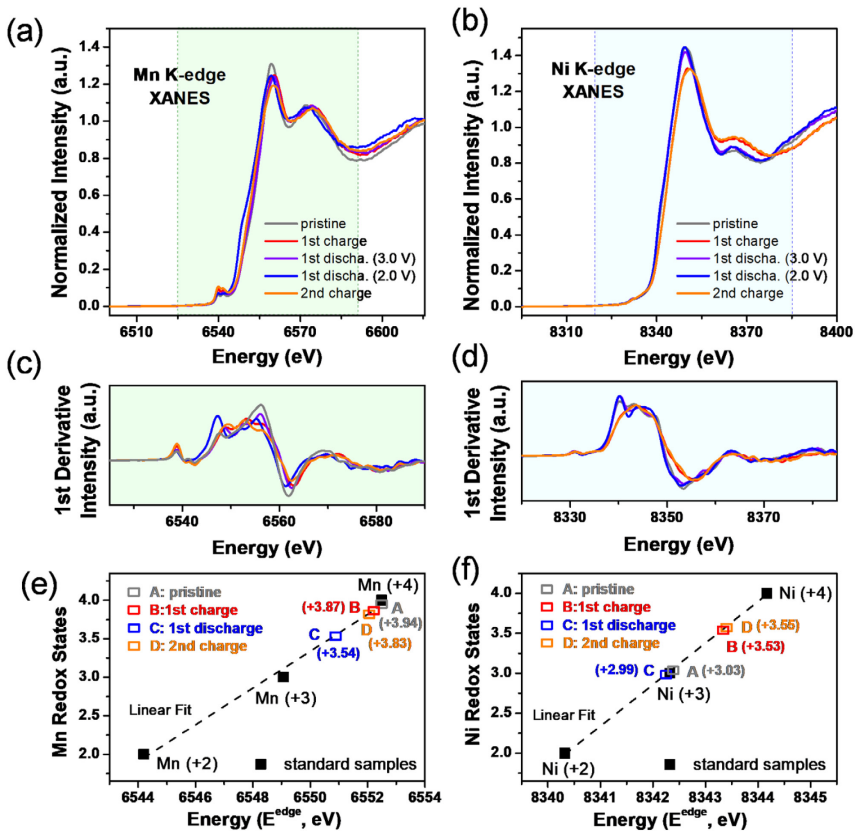

Figure 3. Analysis of cationic states in T2-type LLNMO during the initial two cycles. (a) Mn and (b) Ni K-edge hard X-ray absorption spectra (XAS) of different samples (pristine, 1st charged 4.8 V, 1st discharged 3.0 V, 1st discharged 2.0 V and 2nd charged 4.8 V). Corresponding 1st derivative plots of (c) Mn and (d) Ni K-edge XAS. Besides, these spectra are shown after multiple loss events and background has been subtracted. The evolutions of approximate oxidation states of (e) Mn and (f) Ni during initial two cycles. The relationship between Mn/Ni redox states and the K-edge positions is determined by the integral method.

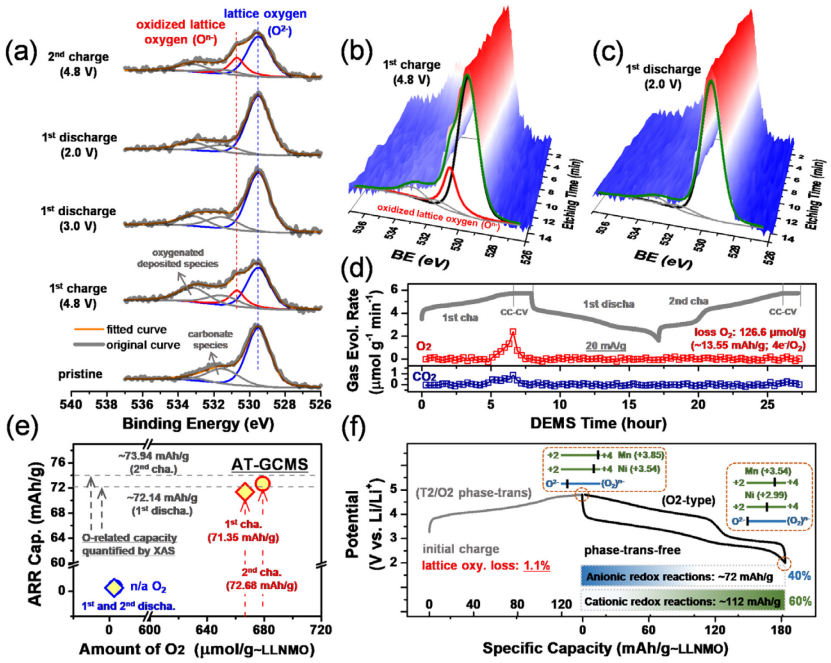

Figure 4. Analysis of O activity in T2-type LLNMO during the initial two cycles. (a) X-ray photoelectron spectra (XPS) of T2-type LLNMO electrode at different states (pristine, 1st charged 4.8 V, 1st discharged 3.0 V, 1st discharged 2.0 V and 2nd charged 4.8 V). XPS patterns of (b) charged and (c) discharged T2-type LLNMO electrode with different etching time. (d) *Operando* differential electrochemical mass spectrometry (DEMS) of the rate of evolution of O_2 and CO_2 during cycling. (e) Results of acid titrations-gas chromatography mass spectrometry (AT-GCMS) of two electrodes harvested at the end of each of the first two charge processes. (f) Capacity contributions of oxygen redox (reversible oxygen behavior, O_2 evolution) and Ni/Mn-based redox reactions during the initial two cycles.

The T2-type $Li_{0.72}[Li_{0.12}Ni_{0.36}Mn_{0.52}]O_2$ displays the ABB′A′ oxygen stacking arrangement and tetrahedral alkali metal site, harvesting the reversible Li migration and stable structural evolution after initial T2/O2 phase transition. The complicated anionic/cationic redox reactions have been distinctly assigned and the corresponding capacity distributions have been well quantified.

Keywords: cathode materials, layered oxides, voltage decay, lattice oxygen release, structural stability

Xin Cao, Haifeng Li, Yu Qiao,* Min Jia, Hirokazu Kitaura, Jianan Zhang, Ping He, Jordi Cabana and Haoshen Zhou*

Structure Design Enables Stable Anionic and Cationic Redox Chemistry in a T2-type Li-excess Layered Oxide Cathode